Data Redundancy and Reduced-Scan Reconstruction in Reflectivity Tomography

Xiaochuan Pan, *Senior Member, IEEE*, Yu Zou, and Mark A. Anastasio, *Member, IEEE*

Abstract—In reflectivity tomography, conventional reconstruction approaches require that measurements be acquired at view angles that span a full angular range of 2π. It is often, however, advantageous to reduce the angular range over which measurements are acquired, which can, for example, minimize artifacts due to movements of the imaged object. Moreover, in certain situations it may not be experimentally possible to collect data over a 2π angular range. In this work, we investigate the problem of reconstructing images from reduced-scan data in reflectivity tomography. By exploiting symmetries in the data function of reflectivity tomography, we *heuristically* demonstrate that an image function can be uniquely specified by reduced-scan data that correspond to measurements taken over an angular interval (possibly disjoint) that spans at least π radians. We also identify sufficient conditions that permit for a stable reconstruction of image boundaries from reduced-scan data. Numerical results in computer-simulation studies indicate that images can be reconstructed accurately from reduced-scan data.

Index Terms—Data redundancy, image reconstruction, reduced scan, reflectivity tomography.

I. INTRODUCTION

REFLECTIVITY tomography has been applied to numerous biomedical [1]–[6] and nondestructive testing [7] imaging problems. In two-dimensional (2-D) reflectivity tomography [8], [9], a weakly reflecting object that is immersed in an acoustically homogeneous background medium is illuminated with infinitesimally short ultrasonic pulses, and the concomitant reflected signals are measured as functions of time at each of the multiple source locations. The task in reflectivity tomography is to reconstruct from such measured data a function describing the reflectivity distribution within the scattering object.[1]

In reflectivity tomography, an imaging configuration that acquires data over the complete angular interval of 2π is referred to as a *full-scan* configuration. Norton derived [8] an analytic algorithm for reconstructing the object function from data acquired with a full-scan configuration. In tomographic imaging, however, it is often desirable to minimize the angular range over which data are acquired. When ionizing radiation is employed, this can reduce the radiation dose that is delivered to the subject during the imaging process. An advantage of reducing the scanning angle, which is also relevant to biomedical imaging applications employing nonionizing radiation, is that the time needed to collect data is reduced, thus diminishing image artifacts and distortions created by movements of the object during the imaging process. Furthermore, in certain situations it may not be experimentally possible to collect data over a full angular range of 2π.

An imaging configuration that acquires data over an angular interval Φ, where $\pi \leq \Phi < 2\pi$, is referred to as a *reduced-scan* configuration. It has been shown that one can accurately reconstruct images from data acquired with reduced-scan configurations in tomographic imaging modalities including fan-beam computed tomography (CT) [10] and single-photon emission computed tomography (SPECT) [11], [12]. A reduced-scan reconstruction problem for reflectivity tomography has also been studied [13]. In that work, which was based on the paraxial approximation [13], an iterative reconstruction algorithm was proposed for (approximately) reconstructing an object function from reduced-scan data. However, it remains unclear whether an object function can be exactly determined from reduced-scan data in reflectivity tomography.

In this work, we investigate the problem of image reconstruction from reduced-scan data in reflectivity tomography. A potato-peeler perspective[2] is proposed for identifying data symmetries in reflectivity tomography. Using the identified data symmetries, we *heuristically* demonstrate that data acquired with reduced-scan configurations in reflectivity tomography are, in principle, sufficient to specify the object function. We also apply results from microlocal analysis [15] to investigate the stability of reconstructing image boundaries from reduced-scan data in reflectivity tomography.

Norton's algorithm [8], which can be applied only to full-scan data, cannot accurately reconstruct images from reduced-scan data. Instead, we propose to use the expectation maximization (EM) algorithm [16] for reconstruction of the object function from reduced-scan data. Using computer-simulation studies, we evaluate the numerical properties of images that are reconstructed from reduced-scan data. The results of

[1]For simplicity, we refer to the object's reflectivity function as the object function.

[2]The potato-peeler perspective is conceptually similar to the so-called "layer-stripping" method for solving the Helmholtz equation, e.g., in impedance imaging [14], in the sense that the object function is determined layer by layer. However, the mathematical formulation of the potato-peeler perspective differs entirely from that of the existing "layer-stripping" method [14]. We are currently developing a mathematical formulation for the potato-peeler perspective for reflectivity tomography and will report such results elsewhere.
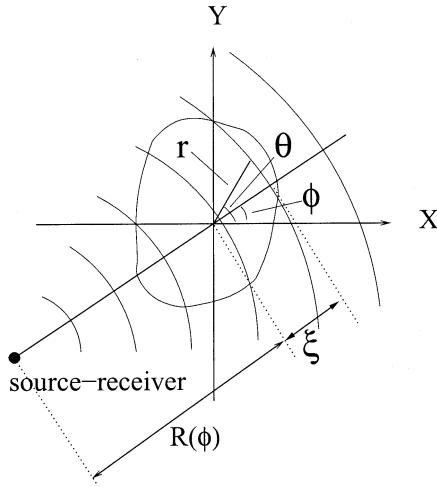
Fig. 1. Schematic illustration of the scanning geometry in reflectivity tomography.

these studies indicate that, under practically relevant conditions, images can be reconstructed accurately from reduced-scan data. In particular, for reflecting objects and scanning configurations that may arise in realistic experiments, numerically accurate images can be reconstructed from reduced-scan data acquired over, e.g., an angular interval of only π.

II. DATA FUNCTION IN REFLECTIVITY TOMOGRAPHY

In this section, we briefly discuss the data function in reflectivity tomography and summarize Norton's algorithm [8] for image reconstruction from full-scan data. Let $f(r, \theta)$ denote a 2-D, bounded, and nonnegative object function with compact support on the disk of radius R_f centered at the origin, for some fixed real number $R_f > 0$. As shown in Fig. 1, the object function is embedded in an acoustically homogeneous background medium, and an omni-directional point source-receiver is located at the polar coordinates $(R, \phi+\pi)$ on a circular source-receiver trajectory curve $\mathcal{C}$ that encloses the object function. At time $t = 0$, an infinitesimally short pulse of sound is emitted from the point source, and the wavefield that is backscattered (i.e., reflected) from the reflecting object is measured at the source location as a function of time.

The measured data can, under certain conditions [9], be interpreted as a set of line integrals of $f(r, \theta)$ defined over all circular arcs (with varying radii) that are centered at a source-receiver location $(R, \phi + \pi)$, where $R_f \leq R$. If this transmit/receive process is repeated for all points on $\mathcal{C}$, multiple sets of these line integrals are obtained. These line integrals can be expressed mathematically as

$$
\begin{aligned}
g(\xi, \phi) = \int_0^{2\pi} d\theta \int_0^{R_f} dr\, r\, f(r, \theta)\delta \\
\times \left(\sqrt{R^2 + r^2 - 2Rr\cos(\phi + \pi - \theta)} - R - \xi \right)
\end{aligned} \quad (1)
$$

where $\xi \in [-R, R]$, and the Dirac δ function restricts the integration over a circular arc with a radius $R + \xi > 0$ and centered at the point $(R, \phi + \pi)$ on the curve $\mathcal{C}$. The reconstruction

problem in reflectivity tomography is to determine the object function $f(r, \theta)$ from knowledge of the data function $g(\xi, \phi)$.

In full-scan reflectivity tomography, because $g(\xi, \phi)$ is measured for all $\phi \in [0, 2\pi)$, one can calculate its Fourier series expansion coefficient as

$$
g_n(\xi) = \frac{1}{2\pi} \int_0^{2\pi} d\phi\, g(\xi, \phi) \mathrm{e}^{-jn\phi}. \quad (2)
$$

The object function can be expressed as a Fourier series,

$$
f(r, \theta) = \sum_{n=-\infty}^{\infty} f_n(r) \mathrm{e}^{jn\theta}, \quad (3)
$$

where $f_n(r) = (1/2) \int_0^{2\pi} d\theta\, f(r, \theta)\mathrm{e}^{-jn\theta}$. Norton [8] showed that $f_n(r)$ (i.e., the object function) can be determined from knowledge of $g_n(\xi)$ (i.e., the full-scan data $g(\xi, \phi)$) as

$$
f_n(r) = \int_0^{\infty} dz\, z \frac{J_n(rz)}{J_n(Rz)} \left[\int_{-R}^{R} d\xi\, \xi \frac{g_n(\xi)J_0(\rho z)}{2\pi\rho} \right] \quad (4)
$$

where $\rho = R + \xi$ and $J_n(\cdot)$ is the nth-order Bessel function of the first kind. Therefore, (2), (3), and (4) provide a recipe for reconstruction of the object function from full-scan data.

III. DATA SYMMETRY AND REDUCTION OF SCANNING ANGLE

Data symmetries have been exploited to demonstrate whether accurate object functions can be reconstructed from reduced-scan data in other tomographic imaging modalities (e.g., fan-beam CT [10] and SPECT [11], [12]). Below, we use the Radon transform of an object function as a data function to illustrate a data symmetry. The Radon transform of an object function $f(r, \theta)$ is defined as

$$
p(\xi, \phi) = \int_0^{2\pi} d\theta \int_0^{R_f} dr\, r\, f(r, \theta)\delta\left(\xi - r\cos(\phi - \theta)\right) \quad (5)
$$

where $\xi \in [-R_f, R_f]$, and ϕ is the projection angle. A symmetry of the Radon transform exists because its values at conjugate views are identical, i.e.,

$$
p(\xi, \phi) = p(-\xi, \phi + \pi). \quad (6)
$$

Such a symmetry suggests that the full-scan Radon transform contains redundant information. Knowledge of the Radon transform acquired over $[0, \pi)$ can be used for reconstructing an image exactly because knowledge of the Radon transform corresponding to the un-measured angular intervals is fully specified by (6). Inspection of (1) indicates that the data function $g(\xi, \phi)$ in reflectivity tomography possesses no symmetry analogous to that of the Radon transform in (6). However, we reveal below that the data function $g(\xi, \phi)$ does admit symmetries and that such symmetries can be exploited to identify redundant information in full-scan data in reflectivity tomography.
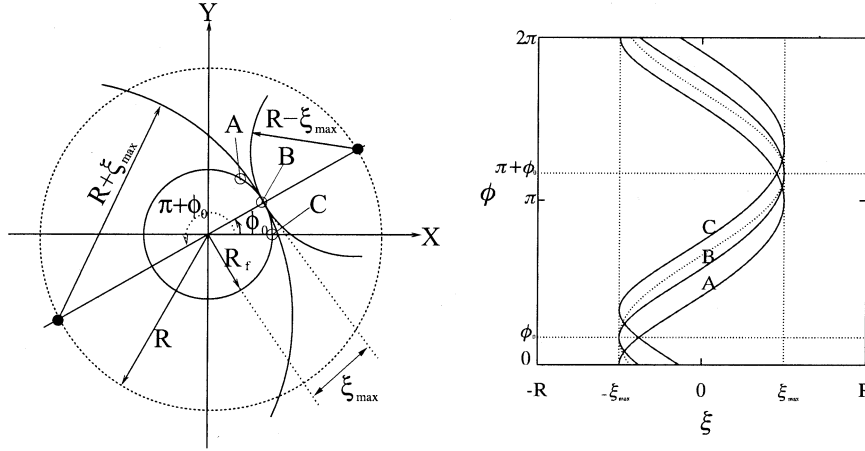
Fig. 2.   Schematic illustration of the measurements at the edge of an object function in reflectivity tomography (left panel). Points A, B, and C in the object function contribute to the measured data on curves with the same labels in the data space (right panel).

A. Potato-Peeler Perspective for Reflectivity Tomography

Although the data function in (1) does not admit a simple symmetry analogous to that of the Radon transform in (6), the fact that the imaging transform in (1) is linear and that $f(r, \theta)$ has a compact support can facilitate the explicit identification of data symmetries in reflectivity tomography. We generalize the potato-peeler perspective, which was developed previously for analyzing data symmetry in SPECT [17], to investigate data symmetries in reflectivity tomography. It should be emphasized that this perspective, to be presented below, is not intended as a mathematically stable and computationally practical reconstruction algorithm. Instead, it is used only for *heuristically* revealing data symmetries in reflectivity tomography.

Without loss of generality, as shown in Fig. 2, we assume that the nonzero support of $f(r, \theta)$ is a disk of radius R_f centered at the origin, i.e., $f(r, \theta) \neq 0$ for $r \leq R_f$ and $f(r, \theta) = 0$ for $r > R_f$. (The procedures and discussion to be presented below can, however, readily be modified to address any compactly supported object functions.) We use $L(\xi, \phi)$ to denote the circular integrating line in (1).

At a given view angle ϕ_0, one can identify a value $\xi_{max} \geq 0$ such that $g(\xi_{max}, \phi_0) \neq 0$ and $g(\xi, \phi_0) = 0$ for $\xi > \xi_{max}$. The assumption on the support compactness of $f(r, \theta)$ indicates that

$$\xi_{max} = R_f. \tag{7}$$

Therefore, one can determine R_f from knowledge of ξ_{max}. Conceptually, we treat $f(r, \theta)$ a collection of weighted 2-D Dirac delta functions.[3] Because the integrating line $L(\xi_{max}, \phi_0)$ intersects $f(r, \theta)$ only at the single point (R_f, ϕ_0) (i.e., point B in Fig. 2(a)), (1) reduces to

$$g(\xi_{max}, \phi_0) = f(R_f, \phi_0). \tag{8}$$

On the other hand, at the conjugate view angle $\phi_0 + \pi$, one can identify a same value $\xi_{max} \geq 0$ such that $g(-\xi_{max}, \phi_0 + \pi) \neq 0$ and $g(-\xi, \phi_0 + \pi) = 0$ for $\xi > \xi_{max}$. In this situation, the integrating line $L(-\xi_{max}, \phi_0 + \pi)$ also intersects only at a single

[3]i.e., $f(r, \theta) = \int_0^{2\pi} d\theta' \int_0^{R_f} dr' r' f(r', \theta') (\delta(r - r') \delta(\theta - \theta')/r')$.

point (R_f, ϕ_0) [i.e., point B in Fig. 2(a)] on the outermost edge of the support. Again, as a result, (1) reduces to

$$g(-\xi_{max}, \phi_0 + \pi) = f(R_f, \phi_0). \tag{9}$$

Therefore, the object function $f(r, \theta)$ at the outermost point (R_f, ϕ_0) (i.e., point B in Fig. 2(a)) can be specified completely by either one of the two measurements $g(\xi_{max}, \phi_0)$ and $g(-\xi_{max}, \phi_0 + \pi)$.

The component of $f(r, \theta)$ corresponding to the point (R_f, ϕ_0) produces [via (1)] a component of the data function given by

$$g_B(\xi, \phi) = g(\xi_{max}, \phi_0) I(\xi, \phi) \tag{10}$$

where $I(\xi, \phi)$ is an indicator function defined as $I(\xi, \phi) = 1$ for $\xi = [R_f^2 + R^2 - 2R_f R \cos(\phi + \pi - \phi_0)]^{(1/2)} - R$ and $I(\xi, \phi) = 0$ otherwise. As shown in Fig. 2(b), the function $I(\xi, \phi)$ specifies the loci of points in the data space that receive a contribution when $f(r, \theta)$ in (1) is replaced by $f(R_f, \phi_0)((\delta(r - R_f)\delta(\theta - \phi_0))/r)$. From $g(\xi, \phi)$ and $g_B(\xi, \phi)$, one can obtain a new data function as

$$\hat{g}(\xi, \phi) = g(\xi, \phi) - g_B(\xi, \phi) \tag{11}$$

which contains no contributions from point B in the object function. In a similar manner, all points (e.g., points A and C) on the outermost edge of $f(r, \theta)$ can be determined and "peeled away", and their contributions to the data function $g(\xi, \phi)$ can be removed, each time forming a new data function. The next set of points at the interior of the object function will be exposed. By the same procedure, the next layer of the object function can be determined and "peeled away," and their contributions to the new data function can be removed. By repeating this procedure, one can determine $f(r, \theta)$ by completely peeling, layer by layer, the object function away.

B. Reduction of Scanning Angle

From (8) and (9), one can readily identify a symmetry of the data function as

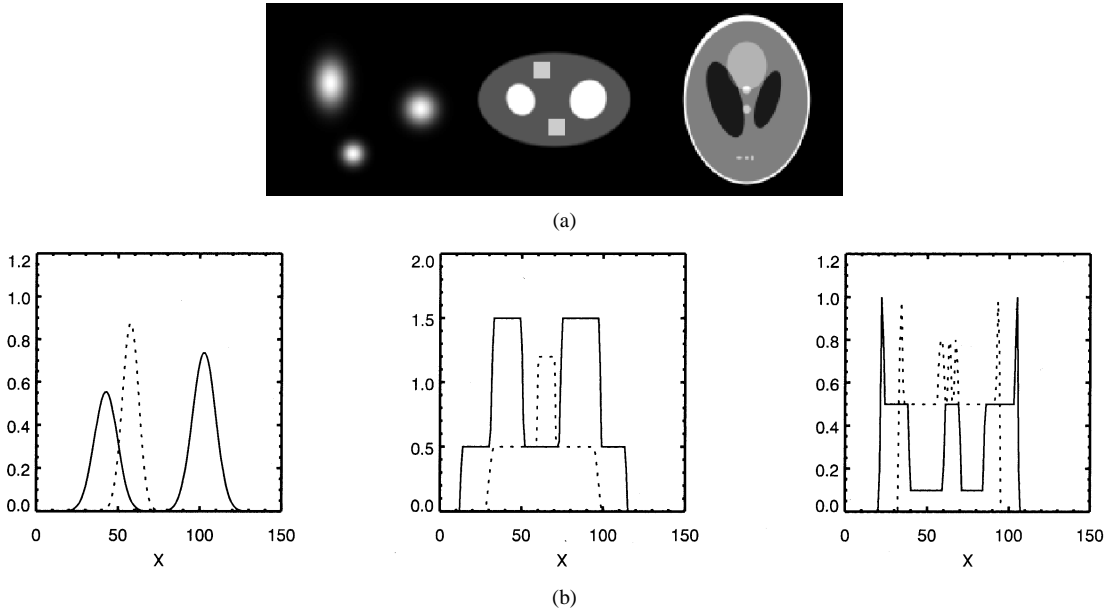$$g(\xi_{max}, \phi_0) = g(-\xi_{max}, \phi_0 + \pi). \tag{12}$$

(a)

(b)

Fig. 3. (a) Numerical phantoms used in simulation studies. The phantom in the left panel, which is referred to as the Gaussian phantom, is comprised of three Gaussian functions, representing a smooth object function. The phantoms in the middle and right panels, which contain boundaries (i.e., discontinuities), are referred to as the ellipse and Shepp-Logan phantoms, respectively. (b) Profiles through the Gaussian, ellipse, and Shepp-Logan phantoms. The solid lines correspond to horizontal profiles through the centers ($y = 64$) of the phantoms. The dotted lines represent horizonal profiles along the line $y = 30$ for the Gaussian phantom, $y = 40$ for the ellipse phantom, and $y = 25$ for the Shepp-Logan phantom.

Furthermore, using the potato-peeler perspective described above, one can identify a symmetry of $\hat{g}(\xi, \phi)$ as

$$\hat{g}(\xi_m, \phi) = \hat{g}(-\xi_m, \phi + \pi) \qquad (13)$$

where $\hat{g}(\xi_m, \phi) \neq 0$ and $\hat{g}(-\xi_m, \phi + \pi) \neq 0$ for $0 \leq \xi_m \leq \xi_{max}$, and $g(\xi, \phi) = 0$ for $|\xi| > \xi_m$. The symmetry condition in (13) indicates that any point of the object function can be specified by the values of a (processed) data function $\hat{g}(\xi, \phi)$ at conjugate views. As a result, the potato-peeler perspective suggests that the object function may be specified by knowledge of the measured data $g(\xi, \phi)$ available over $\phi \in [0, \pi)$. We refer to a scanning configuration that acquires $g(\xi, \phi)$ over $\phi \in [0, \pi)$ as the *short-scan* configuration. More generally, the potato-peeler perspective indicates that an object function may be specified by knowledge of data $g(\xi, \phi)$ measured over $\phi \in \Phi$, where Φ is any proper subset of $[0, 2\pi)$ such that $\phi' \in \Phi$ OR $\phi' + \pi \in \Phi$, for all $\phi' \in [0, \pi)$. We refer to a scanning configuration that acquires data at $\phi \in \Phi$ as a π-*scheme* configuration [12]. Obviously, the short-scan configuration can be viewed as a special case of the π-scheme configurations. The data symmetries above indicate that full-scan data in reflectivity tomography contain redundant information that can be exploited for reducing the angular range over which measurements need to be acquired.

By use of the potato-peeler perspective, it was revealed heuristically above that an object function $f(r, \theta)$ in reflectivity tomography can be specified uniquely by knowledge of short-scan or π-scheme data. This is consistent with the result of an analysis of a family of Radon transforms over circles [18]. One can use principles from microlocal analysis [15], [19], as described in Appendix A, to derive theoretically sufficient conditions for stable reconstruction of boundaries (more generally, singularities) in the object function. One of the sufficient conditions suggests that all boundaries in the

object function can stably be reconstructed from data acquired over $[0, 3\pi/2)$. Also, as discussed in Appendix A, depending upon the boundary locations within an object function, it is theoretically possible that all boundaries can stably be recovered from short-scan or π-scheme data. More important, as the results of numerical studies below show, under realistic practical conditions (e.g., in the presence of data noise), images reconstructed from short-scan or π-scheme data generally appear to be comparable to those obtained from full-scan data.

IV. RESULTS

Using simulation studies, we numerically investigated the accuracy of images reconstructed from reduced-scan data in reflectivity tomography.

A. Data and Reconstruction Algorithm

We used three different numerical phantoms, which are shown in Fig. 3(a), to generate simulated measurement data corresponding to the imaging transform in (1). The phantom in the left panel of Fig. 3(a) is comprised of three 2-D Gaussian functions, representing a smooth object function containing no boundaries, whereas the phantoms in the middle and right panels of Fig. 3(a) contain boundaries and complex structures. We refer to the two phantoms in the left and middle panels of Fig. 3(a) as the Gaussian phantom and the ellipse phantom, respectively. The phantom on the right panel, known as the Shepp-Logan phantom, is widely used in the medical imaging community. Profiles through the Gaussian, ellipse, and Shepp-Logan phantoms are shown in Fig. 3(b). The solid lines correspond to horizontal profiles through the centers ($y = 64$) of the phantoms. The dotted lines represent horizontal profiles along the line $y = 30$ for the Gaussian phantom (far-left), $y = 40$ for the ellipse phantom (center), and $y = 25$ for the
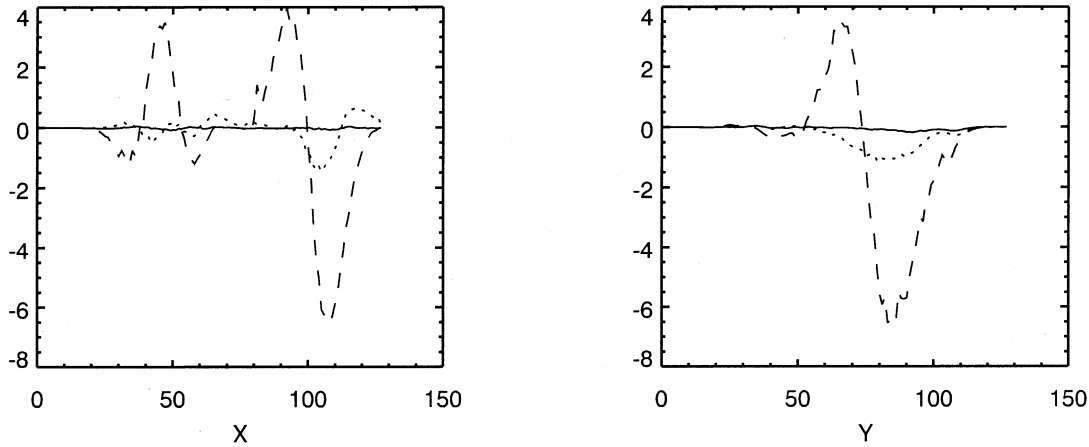
Fig. 4. Profiles through difference images at $x = 64$ (left) and $y = 44$ (right) obtained from data acquired over $[0, \pi)$ (solid), $[0, 3\pi/4)$ (dotted), and $[0, \pi/2)$ (dashed).

Shepp–Logan phantom (far right). When we simulated the measured data, the phantoms were centered at the origin of the $x - y$ coordinate system, which was also the center of the circular source-receiver trajectory (see Fig. 1). The data function $g(\xi, \phi)$ was sampled at 128 evenly spaced values of ξ and 120 angles ϕ that were evenly spaced over the interval $[0, 2\pi)$. The matrix size of the reconstructed images is 128 × 128.

It remains unclear whether analytic algorithms exist for accurate reconstruction of images from reduced-scan data. In this work, we use the EM algorithm [16] for image reconstruction. For notational convenience, let $x = (r, \theta)$ and $y = (\xi, \phi)$ denote 2-D vectors in the image and data spaces, respectively. Equation (1) can then be expressed as

$$g(y) = \int_{D_x} dx\, h(x, y) f(x) \quad \forall y \in D_y \tag{14}$$

where the real and nonnegative functions $g(y)$ and $f(x)$ denote the data and object functions that are supported on the domains D_y and D_x, respectively. (For instance, for a short-scan configuration, $D_y = \{y | -R \leq \xi \leq R, \phi \in \pi\}$.) The kernel $h(x, y)$ of the imaging transformation is given by

$$h(x, y) = \delta\left([r^2 + R^2 - 2rR\cos(\phi - \theta)]^{\frac{1}{2}} - R - \xi\right). \tag{15}$$

We use

$$f^{(n+1)}(x) = \frac{f^{(n)}(x)}{\int_{D_y} dy\, h(x, y)} \int_{D_y} dy\, \frac{h(x, y) g(y)}{\int_{D_x} dx\, h(x, y) f^{(n)}(x)} \tag{16}$$

as the estimate of the object function, where n is the number of iterations. The initial image $f^{(0)}(x, y)$ is often chosen as a nonzero constant function. The EM algorithm has been shown to yield the maximization-likelihood solution to (14) when the data function $(g(y))$ contain Poisson noise [20]. From a practical point of view, the EM algorithm is easy to implement because it involves only forward and backward transformations between the image and data spaces. In our work, in an attempt to enhance the computational efficiency, we utilized an ordered-subsets [21] implementation of the EM algorithm.

B. Reconstruction of Smooth Object Functions

We first investigated the accuracy of reconstructed images of a smooth object function containing no boundaries. To do so, we used the Gaussian phantom in Fig. 3(a) to generate three noiseless data sets containing measurements over the angular ranges of $[0, \pi/2)$, $[0, 3\pi/4)$, and $[0, \pi)$. The radius of the source-receiver trajectory was taken to be $R = r_0$, where r_0 represents half of the image-array size. From the three data sets, we reconstructed images and, in each case, calculated a difference image between the reconstructed image and the Gaussian phantom.

In Fig. 4, we display profiles through the three difference images at $x = 64$ and $y = 44$ obtained from the $[0, \pi/2)$, $[0, 3\pi/4)$, and $[0, \pi)$ data sets, respectively. It can be observed that the difference profiles obtained from the $[0, \pi)$ data set are almost zero. Because the Gaussian phantom studied has no obvious symmetries, such an observation appears to suggest that an accurate image of a smooth object function can be reconstructed from short-scan data.[4] It can also be seen in Fig. 4 that the difference profiles calculated from the $[0, \pi/2)$ and $[0, 3\pi/4)$ data sets are significantly different from zero, suggesting that accurate images cannot be reconstructed from data acquired over angular intervals less than π.

C. Reconstruction of Images Containing Boundaries

For the ellipse and Shepp–Logan phantoms that contain boundaries, we generated simulated data sets containing measurements over angular ranges $[0, \pi/2)$, $[\pi, 2\pi)$, $[\pi/3, 2\pi/3] \cup [\pi, 4\pi/3] \cup [5\pi/3, 2\pi]$, $[0, 3\pi/2)$, and $[0, 2\pi)$, as shown in Fig. 5. The second and third configurations correspond to short-scan and π-scheme configurations, whereas the last configuration is the full-scan configuration. For each of the ellipse and Shepp–Logan phantoms and for each of the scanning configurations in Fig. 5, we generated two sets of noiseless data by use of two circular source-receiver trajectories with different radii. Using these noiseless data as the means, we generated the corresponding noisy data by adding Gaussian noise.

---

[4]In reflectivity tomography, the stable reconstruction of smooth components of an object function can be deduced by exploiting a correspondence between the Sobolev wavefront sets of the data and object functions [22], [23].
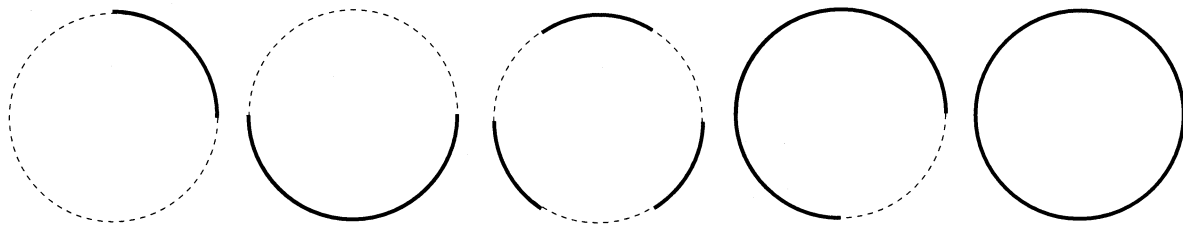
Fig. 5.   Scanning configurations that acquire data over angular intervals $[0, \pi/2)$ (left), $[\pi, 2\pi)$ (second from left), $[\pi/3, 2\pi/3] \cup [\pi, 4\pi/3] \cup [5\pi/3, 2\pi]$ (middle), $[0, 3\pi/2)$ (second from right), and $[0, 2\pi)$ (right). The configurations in the second, third, and fifth panels are also referred to as the short-scan, π-scheme, and full-scan configurations, respectively.
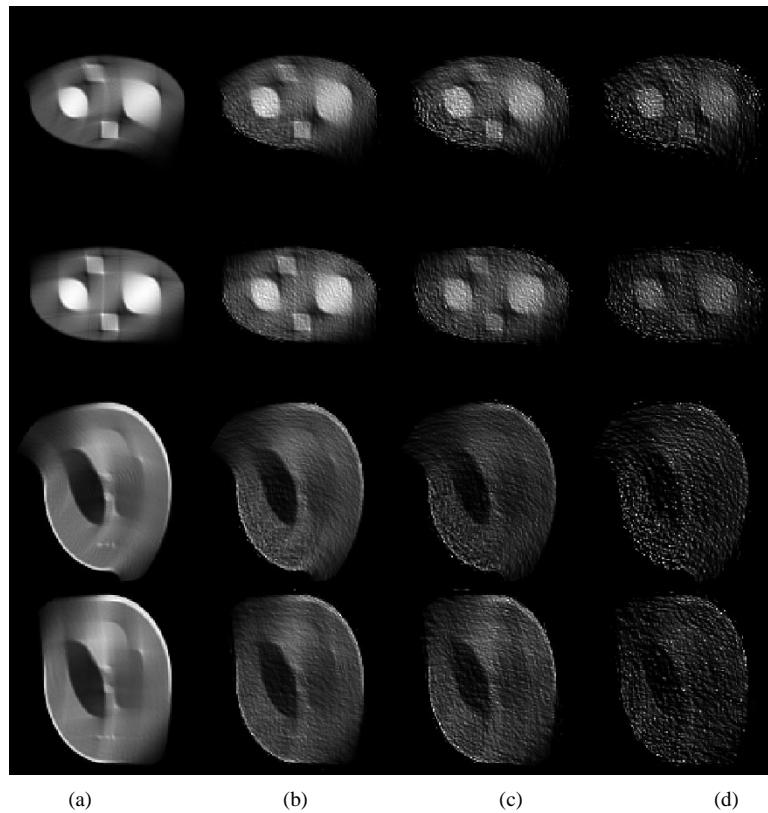

(a)   (b)   (c)   (d)

Fig. 6.   Images reconstructed from noiseless and noisy data acquired over $[0, \pi/2)$ for the ellipse and Shepp-Logan phantoms. The radii of the source-receiver trajectory were set to r_0 in (a) and (c), and $3r_0$ in (b) and (d). Images in the first column were reconstructed from noiseless data, and images in the second, third, and fourth columns were reconstructed from data containing three different levels of Gaussian noise. All of these images contain significant distortions, suggesting that images cannot accurately be reconstructed from data acquired over angular intervals less than π.

In Fig. 6, we display images reconstructed from noiseless and noisy data acquired over $[0, \pi/2)$ (see the configuration in the far left panel of Fig. 5). Clearly, all of the images contain significant distortions, suggesting that images cannot be reconstructed accurately from data acquired over an angular interval less than π. This observation is consistent with that for smooth images above.

For the ellipse phantom, we show in Figs. 7 and 8 images reconstructed from data acquired over angular ranges $[\pi, 2\pi)$, $[\pi/3, 2\pi/3] \cup [\pi, 4\pi/3] \cup [5\pi/3, 2\pi]$, $[0, 3\pi/2)$, and $[0, 2\pi)$. The radii of the source-receiver trajectory for obtaining the results in Figs. 7 and 8 were r_0 and $3r_0$, respectively, where r_0 represents half of the image-array size. Images reconstructed from noiseless data are shown in the first columns in Figs. 7 and 8. The overall visual quality of the noiseless images reconstructed from short-scan or π-scheme data appears comparable to that obtained from full-scan data. In particular, for the case

of $R = 3r_0$ (Fig. 8), which may correspond to a typical realistic experimental geometry, the noiseless images reconstructed from the short-scan and π-scheme data appear to be virtually identical to that reconstructed from the full-scan data. Images in the second, third, and fourth columns in Figs. 7 and 8 were reconstructed from data containing Gaussian noise with standard deviations of 1, 2, and 4, respectively. These noisy images appear distinct, but are not qualitatively different (for a given noise level). Differences in the statistical characteristics of the images (i.e. the appearance of the image noise) are to be expected because the same reconstruction algorithm is applied to different noisy data sets. Furthermore, the full-scan data contain redundant information that is not present in the short-scan or π-scheme data, which serves to effectively average out certain components of the data noise.

For the Shepp-Logan phantom, we show images in Figs. 9 and 10 reconstructed from data acquired over angular ranges
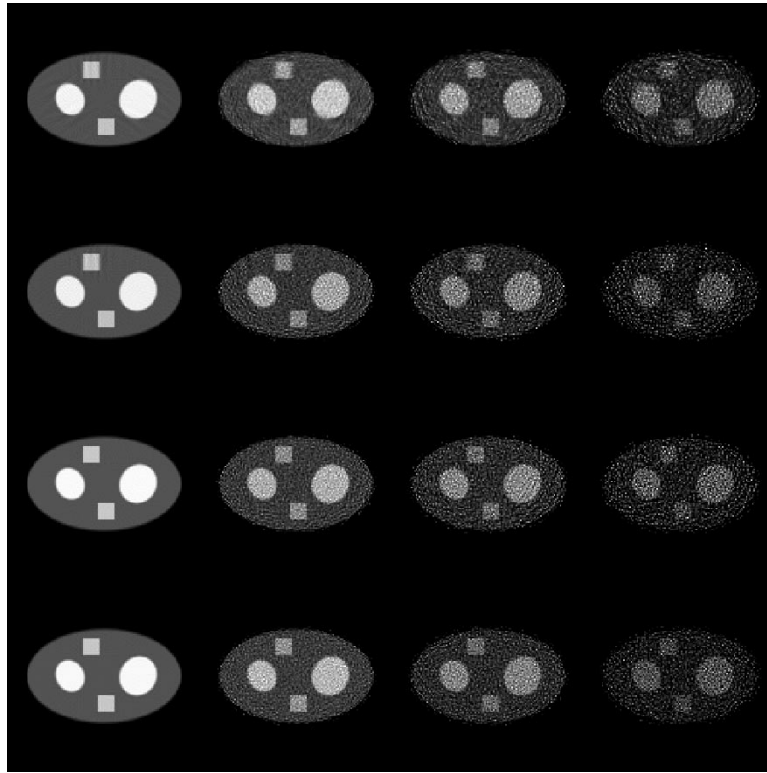
Fig. 7. Images reconstructed for the ellipse phantom from data acquired over angular intervals $[\pi, 2\pi)$ (1st row), $[\pi/3, 2\pi/3] \cup [\pi, 4\pi/3] \cup [5\pi/3, 2\pi]$ (2nd row), $[0, 3\pi/2)$ (3rd row), and $[0, 2\pi)$ (4th row). The radius of the source-receiver trajectory is r_0. Images in the first column were reconstructed from noiseless data, and images in the second, third, and fourth columns were reconstructed from data containing three different levels of Gaussian noise.

Fig. 8. Images reconstructed for the ellipse phantom from data acquired over angular intervals $[\pi, 2\pi)$ (1st row), $[\pi/3, 2\pi/3] \cup [\pi, 4\pi/3] \cup [5\pi/3, 2\pi]$ (2nd row), $[0, 3\pi/2)$ (3rd row), and $[0, 2\pi)$ (4th row). The radius of the source-receiver trajectory is $3r_0$. Images in the first column were reconstructed from noiseless data, and images in the second, third, and fourth columns were reconstructed from data containing three different levels of Gaussian noise.
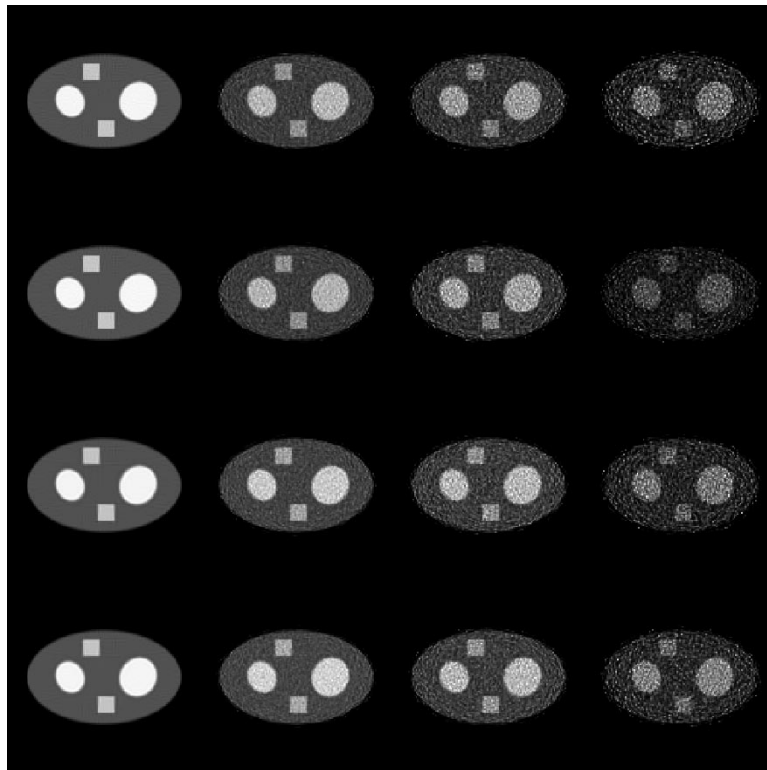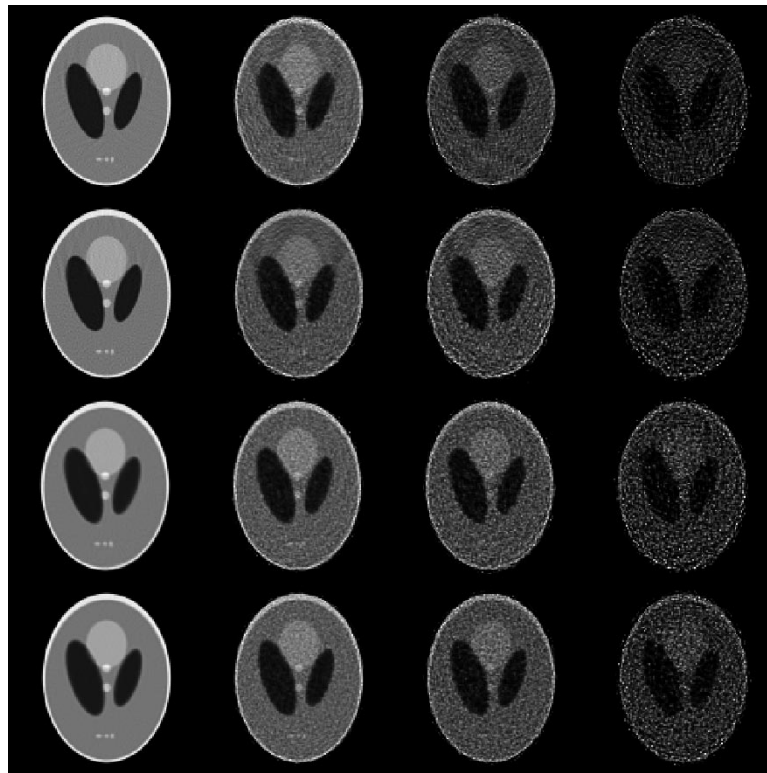
Fig. 9. Images reconstructed for the Shepp-Logan phantom from data acquired over angular intervals $[\pi, 2\pi)$ (1st row), $[\pi/3, 2\pi/3] \cup [\pi, 4\pi/3] \cup [5\pi/3, 2\pi]$ (2nd row), $[0, 3\pi/2)$ (3rd row), and $[0, 2\pi)$ (4th row). The radius of the source-receiver trajectory is r_0. Images in the first column were reconstructed from noiseless data, and images in the second, third, and fourth columns were reconstructed from data containing three different levels of Gaussian noise.

$[\pi, 2\pi)$, $[\pi/3, 2\pi/3] \cup [\pi, 4\pi/3] \cup [5\pi/3, 2\pi]$, $[0, 3\pi/2)$, and $[0, 2\pi)$, respectively. The radii of the source-receiver trajectory for obtaining the results in Figs. 9 and 10 were r_0 and $3r_0$, respectively. Images reconstructed from noiseless data are shown in the first columns of Figs. 9 and 10, and images in the second, third, and fourth columns in Figs. 9 and 10 were reconstructed from data containing Gaussian noise with standard deviations of 1, 2, and 4, respectively. Again, for images in Figs. 9 and 10, one can make observations similar to those for images in Figs. 7 and 8. The overall visual quality of the images reconstructed from short-scan or π-scheme data appears comparable to that obtained from the full-scan data, and images reconstructed from various noisy data sets appear qualitatively similar (for a given noise level).

According to microlocal analysis [15], certain image boundaries may not theoretically be reconstructed stably from short-scan or π-scheme data. For example, in the short-scan case in which the source-receiver trajectory is within the lower half plane (see the configuration in the second panel in Fig. 5), the microlocal analysis suggests that vertical boundaries in the ellipse phantom that reside in the upper half plane cannot be reconstructed stably. This is because the normal vectors of such vertical boundaries do not intersect the source-receiver trajectory in the lower half plane. From the noiseless image in the far left panel of the first row in Fig. 7, one can see artifacts near the vertical boundaries of the square region in the upper half. However, it is interesting to observe that such artifacts do not appear to be prominent. Furthermore, as the radius of the source-receiver trajectory

increases, such artifacts become almost undetectable numerically, as confirmed by the virtually artifact-free noiseless images in the far left panels of the first and second rows in Fig. 8 for the case $R = 3r_0$.

The boundaries in the images in the far left panels of the third rows in Figs. 7–10 appear identical to those displayed in the far left panels of the fourth rows in Figs. 7–10. This confirms our assertion (see Appendix A) that image boundaries can stably be reconstructed from data acquired over an angular range of $3\pi/2$. As images in the second, third, and fourth columns in Figs. 7–10 show, for a given noise level, image boundaries reconstructed from noisy data acquired with the reduced-scan and full-scan data appear qualitatively similar.

For completeness, we also used Norton's algorithm [(2), (3), and (4)] to reconstruct images of the Shepp-Logan phantom from data that are acquired with the short-scan and full-scan configurations in which the radius of the source-receiver trajectory is $3r_0$. Images reconstructed from short-scan and full-scan data are shown in the first and second rows in Fig. 11, respectively. Noiseless images are shown in the first columns in Fig. 11, whereas noisy images shown in the second, third, and fourth columns in Fig. 11 were reconstructed from data containing Gaussian noise with standard deviations of 1, 2, and 5, respectively. As expected, images reconstructed from short-scan data contain significant artifacts. Also, images reconstructed from full-scan data contain slight ringing artifacts and have poorer resolution as compared to those obtained with the EM algorithm, suggesting that Norton's algorithm is susceptible to numerical errors.
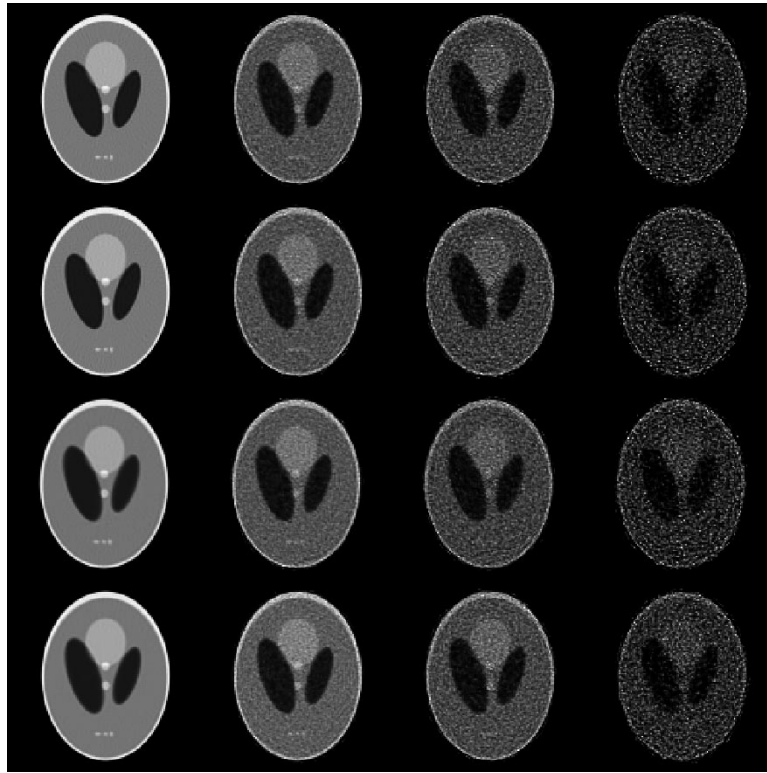
Fig. 10.   Images reconstructed for the Shepp-Logan phantom from data acquired over angular intervals $[\pi, 2\pi)$ (1st row), $[\pi/3, 2\pi/3] \cup [\pi, 4\pi/3] \cup [5\pi/3, 2\pi]$ (2nd row), $[0, 3\pi/2)$ (3rd row), and $[0, 2\pi)$ (4th row). The radius of the source-receiver trajectory is $3r_0$. Images in the first column were reconstructed from noiseless data, and images in the second, third, and fourth columns were reconstructed from data containing three different levels of Gaussian noise.
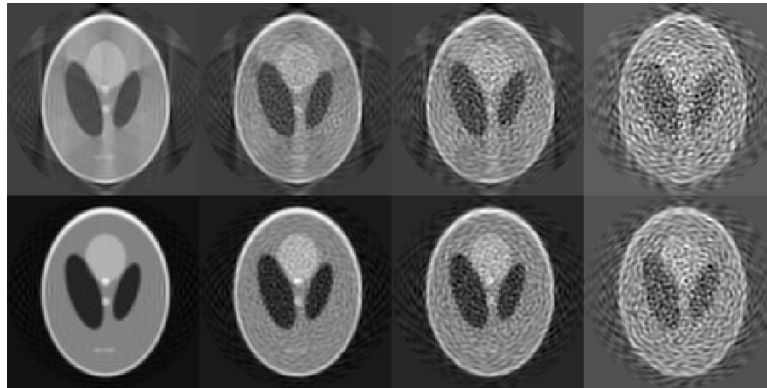

Fig. 11.   Images reconstructed by use of Norton's algorithm from short-scan data (1st row) and full-scan data (2nd row) that were acquired with a circular source-trajectory of radius $R = 3r_0$. Images in the first column were reconstructed from noiseless data, and images in the second, third, fourth columns were reconstructed from data containing three different levels of Gaussian noise.

V. DISCUSSION

In this work, we used a potato-peeler perspective to investigate data symmetries in reflectivity tomography. Based upon the identified data symmetries, we showed heuristically that an object function with a compact support can be specified by knowledge of half of the full-scan data. This observation has led to the development of reduced-scan configurations such as short-scan and π-scheme configurations in reflectivity tomography. Reduced-scan reflectivity tomography not only poses a theoretically interesting reconstruction problem, but also has practical implications. For example, in certain situations, it may not be experimentally possible to collect data over a full angular range

of 2π, thus demanding reduced-scans. A unique feature of the potato-peeler perspective is that it provides informative insights into a complex mathematical problem in a conceptually straightforward manner. We also employed the results of microlocal analysis to analyze theoretically the stability of reconstructing image boundaries from reduced-scan data, and we derived theoretically sufficient conditions on reduced-scan configurations which acquire data for accurate reconstruction of an object function.

As predicted by microlocal analysis, certain image boundaries cannot stably be reconstructed from short-scan or π-scheme data in reflectivity tomography. Although artifacts due to the unstable boundary reconstruction can be observed,

such artifacts appear generally weak and become difficult to discern when the data contain noise and/or when the radius R of the source-receiver trajectory becomes large. For example, for $R = 3r_0$, such artifacts were virtually undetectable for the ellipse and Shepp-Logan phantoms studied. This is significant because the ellipse phantom containing the square structures was specifically designed to reveal the possible instabilities of boundary reconstruction in short-scan reflectivity tomography predicted by the microlocal analysis, and because the Shepp-Logan phantom is sufficiently complex to represent many real-world reflecting objects that may be of practical interest. Conceptually, these results might be explained by the fact that the data are becoming more "Radon-like" as the radius R of the source-receiver trajectory increases. (In the limit $R \to \infty$, (1) reduces to the Radon transform, and an exact image can be reconstructed from short-scan or π-scheme data.) Our numerical results have important practical implications: For many reflecting objects possessing boundaries and for scanning configurations with different R that may arise in realistic experiments, images reconstructed from reduced-scan data, such as the short-scan and π-scheme data, can have a numerical accuracy similar to that of full-scan images. The numerical results also verified the sufficient condition that all image boundaries can stably be reconstructed from reduced-scan data taken over an angular range of $3\pi/2$. For smooth object functions, our numerical results suggest that images can be reconstructed accurately from short-scan and π-scheme data.

We are currently developing a mathematical formulation for the potato-peeler perspective for reflectivity tomography and will report such results elsewhere. The perspectives and methods utilized in this work can readily be extended to investigation of, e.g., reconstruction problems in reflectivity tomography for which the source-receiver trajectory is not a circular curve, but is a general curve satisfying certain conditions. This work is also relevant to generalized Radon transforms that integrate over certain (noncircular) curves and to exterior reconstruction problems. In addition to certain pure ultrasound-based imaging modalities, the mathmatical model used in reflectivity tomography may be relevant to emerging imaging techniques such as thermoacoustic computed tomography [24]. Investigation of these topics is currently under way.

APPENDIX

STABILITY OF RECONSTRUCTING IMAGE BOUNDARIES FROM REDUCED-SCAN DATA

Microlocal analysis [19], [23], [25] can be employed for examining whether image boundaries can stably be reconstructed from reduced-scan data in reflectivity tomography. Without loss of generality, we consider boundary reconstruction from short-scan data acquired with the configurations shown in Fig. 12, where the source-receiver trajectories are semi-circles of radii R residing in the lower half plane. According to the microlocal analysis [15], a boundary can stably be reconstructed if and only if the normal vector at that boundary intersects the source-receiver trajectory [22]. For example, as shown in
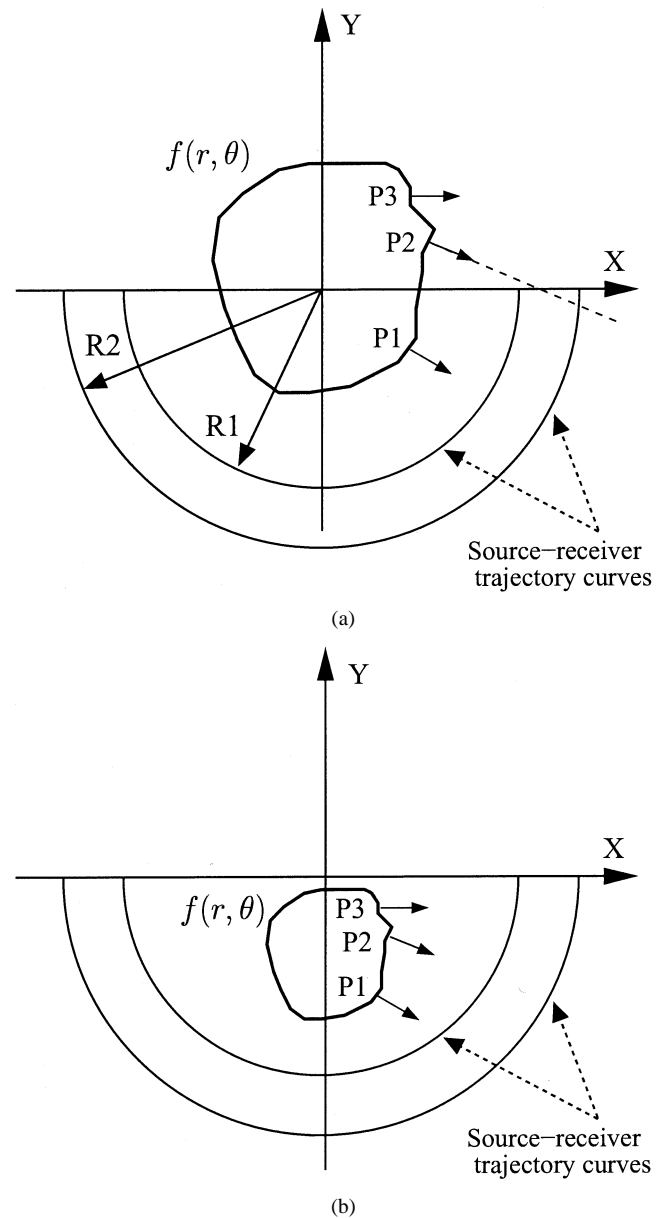

Fig. 12. Short-scan configurations and boundaries in the objects. (a) Some of the boundaries such as P_2 and P_3 reside in the upper half plane; and (b) the entire object resides in the lower half plane and is enclosed by the source-receiver trajectory.

Fig. 12(a), assume $R = R_1$, and consider the three boundaries labeled P_1, P_2, and P_3. The normal vector at boundary P_1 intersects the source-receiver trajectory, and therefore boundary P_1 can stably be reconstructed. However, because the normal vectors at boundaries P_2 and P_3 do not intersect the trajectory with a radius R_1, boundaries P_2 and P_3 cannot stably be reconstructed. If the radius of the source-receiver trajectory is increased to be large enough, the normal vectors that are not parallel to the x-axis will eventually intersect the trajectory, and the number of boundaries that can stably be reconstructed will increase. For example, as shown in Fig. 12, when $R = R_2$, boundary P_2 can now be reconstructed stably. Therefore, when one reconstructs an image from short-scan data in reflectivity tomography, the manifestation of artifacts due to boundaries that cannot be stably reconstructed would depend on the

magnitude of R. Notice that the normal vector at boundary P_3 is parallel to the x-axis, and will therefore never intersect the source-receiver trajectory with a finite radius in the lower half plane. Therefore, one can conclude that certain boundaries cannot, in theory, be reconstructed stably from short-scan data in reflectivity tomography. Similar conclusions can be made for the stability of boundary reconstruction in π-scheme reflectivity tomography. However, as the results in numerical studies indicated, for object functions with complicated boundaries and for source-receiver trajectories with radii R of practical interest, artifacts due to unstable reconstruction of the boundaries from short-scan and π-scheme data do not appear to be prominent.

Based upon the microlocal analysis, one can derive theoretically sufficient conditions for stable reconstruction of image boundaries. In the limiting case, i.e., $R \rightarrow \infty$, the data function (see (1)) in reflectivity tomography reduces to the Radon transform, and normal vectors of any boundaries will intersect the source-receiver trajectory at infinity. Therefore, all of the boundaries can stably be reconstructed from short-scan or π-scheme Radon data. Also, considering the scanning configuration in the fourth panel of Fig. 5, the source-receiver trajectory of radius R in this configuration covers an angular interval of $3\pi/2$. In this case, it can readily be verified that any normal vectors on image boundaries intersect the source-receiver trajectory. Therefore, one can obtain a sufficient condition that all of the boundaries can stably be reconstructed from data acquired over a reduced angular interval that spans $3\pi/2$. Furthermore, one can design a scanning configuration such that all of the boundaries within an object function can stably be reconstructed from, e.g., the short-scan data. As shown in Fig. 12(b), for the entire object that is placed in the lower half of the plane and is enclosed by the source-receiver trajectory, all boundaries in the object can stably be reconstructed because their normal vectors, in this situation, intersect the source-receiver trajectory.

ACKNOWLEDGMENT

REFERENCES

[1] J. Ylitalo, J. Kaovukangas, and J. Oksman, "Ultrasonic reflection mode computed tomography through a skullbone," *IEEE Trans. Biomed. Eng.*, vol. 37, pp. 1059–1065, 1990.

[2] K. Dines and A. Goss, "Computer ultrasonic reflection tomography," *IEEE Trans. Ultrason., Ferroelect., Freq. Contr.*, vol. 34, pp. 309–317, 1987.

[3] T. Mast, "Wideband quantitative ultrasonic imaging by time-domain diffraction tomography," *J. Acoust. Soc. Amer.*, vol. 106, pp. 3061–3071, 1999.

[4] I. Akiyama and K. Yano, "Synthetic aperture computed tomography acoustical imaging," *Acoust. Imag.*, vol. 23, pp. 575–581, 1997.

[5] I. Akiyama, N. Takizawa, and A. Ohya, "Narrow aperture phased array computed tomography," *Acoust. Imag.*, vol. 25, pp. 163–170, 2000.

[6] N. Takizawa, A. Ohya, and I. Akiyama, "Ultrasonic tomography using arc focusing beam," in *IEEE Ultrasonics Symp. Proc.*, 1998, pp. 1659–1662.

[7] M. Moshfeghhi, "Ultrasound reflection-mode tomography using fan-shaped-beam in-sonification," *IEEE Trans. Ultrason., Ferroelect., Freq. Contr.*, vol. 33, pp. 299–314, 1986.

[8] S. Norton, "Reconstruction of a two-dimensional reflecting medium over a circular domain: exact solution," *J. Acoust. Soc. Amer.*, vol. 67, no. 4, pp. 1266–1273, 1980.

[9] S. Norton and M. Linzer, "Ultrasonic reflectivity imaging in three dimensions: exact inverse scattering solutions for plane, cylindrical, and spherical aperatures," *IEEE Trans. Biomed. Eng.*, vol. 28, pp. 202–220, 1981.

[10] D. Parker, "Optimal short scan convolution reconstruction for fanbeam CT," *Med. Phys.*, vol. 9, pp. 254–257, 1982.

[11] F. Noo and J. Wagner, "Image reconstruction in 2D SPECT with 180° acquisition," *Inv. Probl.*, vol. 17, pp. 1357–1371, 2001.

[12] X. Pan, C. M. Kao, and C. E. Metz, "A family of-scheme exponential Radon transforms and the uniqueness of their inverses," *Inv. Probl.*, vol. 18, pp. 825–836, 2002.

[13] C. Lan and W. Xiong, "An iterative method of ultrasonic reflection mode tomography," *IEEE Trans. Med. Imag.*, vol. 13, no. 2, pp. 419–425, 1994.

[14] E. Somersalo, M. Cheney, D. Isaacson, and E. Isaacson, "Layer stripping: a direct numerical method for impedence imaging," *Inverse Problems*, vol. 7, pp. 899–926, 1991.

[15] A. K. Louis and E. T. Quinto, "Local tomographic methods in SONAR," in *Surveys on Solution Methods for Inverse Problems*. New York: Springer-Verlag, 2002.

[16] Y. Vardi and D. Lee, "From image deblurring to optimal investments: maximum likelihood solutions for positive linear inverse problems," *J. R. Statist. Soc. B*, vol. 55, pp. 569–612, 1993.

[17] X. Pan, E. Sidky, C. Kao, Y. Zou, and C. E. Metz, "Image reconstruction in π-scheme SPECT with nonuniform attenuation," IEEE Trans. Nucl. Sci., 2002, submitted for publication.

[18] M. Agranovsky and E. T. Quinto, "Injectivity sts for the Radon transform over circles and complete systems of radial functions," *J. Funct. Anal.*, vol. 139, pp. 383–414, 1996.

[19] E. T. Quinto, "Radon transforms, differential equations, and microlocal analysis," in *Radon Transforms and Tomography*, E. Quinto, L. Ehrenpreis, A. Faridani, F. Gonzalez, and E. Grinberg, Eds: Amer. Math. Soc., 2001, Contemporary Mathematics.

[20] L. A. Shepp and Y. Vardi, "Maximum likelihood reconstruction for emission tomography," *IEEE Trans. Med. Imag.*, vol. MI-1, pp. 113–122, 1982.

[21] H. Hudson and R. Larkin, "Accelerated image reconstruction using ordered subsets of projection data," *IEEE Trans. Med. Imag.*, vol. 13, pp. 601–609, 1994.

[22] E. T. Quinto, Dept. Math., Tufts Univ., Medford, MA, private communication, 2002.

[23] ——, "Singularities of the X-ray transform and limited data tomography in $\mathbf{R}^2$ and $\mathbf{R}^3$," *SIAM J. Math. Anal.*, vol. 24, pp. 1215–1225, 1993.

[24] M. Xu and L. Wang, "Time-domain reconstruction for thermoacoustic tomography in a spherical geometry," *IEEE Trans. Med. Imag.*, vol. 21, pp. 814–822, 2002.

[25] V. Guillemin and S. Sternberg, "Some problems in integral geometry and some related problems in micro-local analysis," *Amer. J. Math.*, vol. 101, pp. 915–955, 1979.

Xiaochuan Pan (M'96–SM'01) received the B.S. degree in physics from Beijing University, China, in 1982, the M.S. degree in physics from the Institute of Physics, Academia Sinica, Taiwan, R.O.C., in 1985, and the M.S. and Ph.D. degrees in physics from the University of Chicago, Chicago, IL, in 1988 and in 1991, respectively.

He is currently an Associate Professor with the Department of Radiology and the Cancer Research Center, University of Chicago. His research effort centers on imaging physics, mathematics, and signal processing and their applications to medical imaging problems.

Yu Zou received the B.S. degree in physics from Beijing University, China, in 1982, and the Ph.D. degree in physics from the Institute of Physics, Academia Sinica, Taiwan, R.O.C., in 1994.

He is currently a Research Associate with the Department of Radiology, University of Chicago, Chicago, IL. His research effort centers on imaging physics and its applications to medical imaging problems. In additional to reflectivity tomography, he has been working on nuclear medicine imaging and helical cone-beam CT.

Mark A. Anastasio (S'89–M'01) recieved the B.S. and M.S.E. degrees in electrical engineering from the Illnois Institute of Technology, Chicago, and the University of Pennsylvania, Philadelphia, respectively, and the M.S. degree in physics from the University of Illinois at Chicago. He received the Ph.D. degree in medical physics from the University of Chicago in 2001.

He is currently an Assistant Professor of biomedical engineering at the Illinois Institute of Technology. His research interests include the development and investigation of tomograhic imaging algorithms, imaging physics, inverse scattering problems, and other inverse problems in imaging.

Dr. Anastasio is a member of OSA and SIAM.